# Enhanced second harmonic generation of gold nanostars: optimizing multipolar radiation to improve nonlinear properties

Jérémy Rouxel, Thanh Ngoc Nguyen, Hong Shen, Sophie Brasselet, Timothée Toury

Research Article | Vol. 27, No. 4 | 18 Feb 2019 | OPTICS EXPRESS 5620
Optics EXPRESS

# Enhanced second harmonic generation of gold nanostars: optimizing multipolar radiation to improve nonlinear properties

JÉRÉMY R. ROUXEL,[1,2,3] THANH NGOC NGUYEN,[1] HONG SHEN,[1] SOPHIE BRASSELET,[4] AND TIMOTHÉE TOURY[1,*]

[1] *ICD-L2N, CNRS FRE 2019, Université de technologie de Troyes, 10004 Troyes, France*
[2] *Laboratory of Ultrafast Spectroscopy, École Polytechnique Fédérale de Lausanne, Lausanne CH-1015, Switzerland*
[3] *Department of Chemistry, University of California, Irvine, California 92697-2025, USA*
[4] *Aix Marseille Univ, CNRS, Centrale Marseille, Institut Fresnel, F-13013 Marseille, France*
[*] *toury@utt.fr*

**Abstract:** We report a detailed investigation on the second harmonic generation (SHG) emission from single 150 nm diameter non-centrosymmetric gold nanoparticles. Polarization-resolved analysis together with scanning electron microscopy images shows that these nanostructures exhibit a unique polarization-sensitive SHG that depends strongly on the particle's shape. An analytical approach based on multipolar analysis is introduced to link SHG properties to the nanoparticles' shape. Those multipolar modes can be probed using polarization-resolved SHG. This multipolar analysis offers a physical picture of the relation between shape (size, symmetries, defects, etc.) and nonlinear polarized optical efficiency.



## 1. Introduction

It is well known that SHG (Second Harmonic Generation) is forbidden in centrosymmetric bulk materials [1–4]. The crystalline lattice of noble metal nanoparticles is, up to a good approximation, centrosymmetric. So, the SHG is locally emitted from the surface where the centrosymmetry is broken [5–7]. The total SHG emission of the nanoparticle results from the coherent addition of these local SHG emitters. Consequently, the overall shape of the nanoparticle plays a significant role in engineering an efficient SHG response. Numerous studies on SHG have focused on noble spherical nanoparticles in which the role of the morphology deviation from ideal spherical shape has been investigated [4, 8–11]. These spherical structures usually give low SHG efficiencies. The shape of the nanoparticle can be optimized to improve SHG efficiency but this feature has remained explored sparsely [12]. On the other side, a large variety of shape has been explored in different studies, such as sharp metal tips [13], periodic nanostructured metal films [14], split-ring resonators [15], T-shaped [15], L-shaped nanoparticles [16, 17], noncentrosymmetric T-shaped nanodimers [18].

In this article, we report investigations on efficient SHG emission by single metallic threefold symmetry nanoparticles, branched stars and nanotriangles, inspired by previous studies on octupolar molecules possessing high hyperpolarizability. It is an interesting textbook case to address the link between shape, size and nonlinear optical properties in these nanoparticles. It has been proven that this high hyperpolarizability is obtained due to the threefold symmetry of the molecular structures [19–23].

A phenomenological model to understand the nonlinear response of the nanoparticles has been constructed. In this model, SHG responses are generated from the nonlinear sources located at a given distance from the particle center. Consequently, this model takes into account the symmetry of the particles as well as its spatial extension, which allows to compare SHG experimental

#347424 https://doi.org/10.1364/OE.27.005620
Journal © 2019 Received 4 Oct 2018; revised 2 Jan 2019; accepted 10 Jan 2019; published 14 Feb 2019

Optics EXPRESS

results with SEM images.

Finally, we develop an analytical approach to physically interpret the experimental results in terms of multipolar contributions. Various experiments have been conducted to measure the multipolar radiation from nanoparticles [24–27] but none of them linked it, to our knowledge, to the efficiency of the nonlinear response nor did use an adequate definition of multipoles as is demonstrated in section 4. The fitting models did not discuss the role of the point spread function (PSF) and the overlapping of the dipole radiation transmitted through the optical system. The link between the model and the system symmetry was also not discuss in-depth, and less accessible. Linking the shape of the nanoparticles to their optical properties through their multipolar radiations offers a clear picture of the relation between geometry and nonlinear polarized efficiencies. This will help to engineer nanoparticles with an optimized shape to enhance a given property. While the overall size of the particle and its symmetry dictates which multipoles are likely to be important in the radiation, the weight of each multipole is controlled by the shape. This explains why stars and triangles, of similar size, material and symmetry, have very different nonlinear behaviors. One would ideally engineer a perfect multipolar emitter to improve nonlinear properties and this can be quantitatively achieved by measuring the multipolar radiation associated with a given shape. It is interesting to note that, when stars possess shape defects, their SHG efficiency is not as intense and becomes comparable to triangles ones. The multipolar description of the radiation for a given shape can highlight how robust the optical properties are regarding deviations from the ideal shape.

## 2. Second harmonic generation efficiency of nanostars

Pure gold nanoparticles have been fabricated by electron beam lithography (EBL), with a branch-structure or a triangular structure, see Fig. 1(a). Single particles were identified by scanning electron microscopy (SEM) image and marked systematically, Fig. 1(a). Their nonlinear optical properties are carried out by polarized SHG microscopy. Figure 1(b) defines the laboratory frame of coordinates and the angle defining the linear polarization of the incoming pulse. Polarimetric graphs (polarization resolved emitted SHG intensity along the $X$ and $Y$ components, Fig. 1(c)) and SHG imaging, Figs. 1(d) and 1(e), provide information on the SHG efficiency of single particles as well as their nonlinear behaviors. More details on the experimental setup are given in Appendix A.

We have investigated the SHG efficiency of nanostars and compared it with triangles and cylinders. Figure 2 shows the measured values of the off-resonant second-order susceptibility $\chi^{(2)}(0)$ for nanostars, nanotriangles and nanocylinders. Details on the measurement of resonant and off-resonant second-order susceptibilities are also provided in appendix B.

We obtain $\chi^{(2)}(0) \sim 24$ pm.V$^{-1}$ for the nanostars, 17 pm.V$^{-1}$ for the nanotriangles and 3 pm.V$^{-1}$ for the nanocylinders. Nanostars and nanotriangles exhibit much higher SHG $\chi^{(2)}$ than centrosymmetric nanocylinders of the same excitation volume. This indicates an improvement of the SHG efficiency by using non-centrosymmetric shapes. Interestingly, even though nanostars and nanotriangles both possess threefold symmetry, nanostars exhibit higher $\chi^{(2)}$ values than nanotriangles. We will show that this can be interpreted in terms of better spatial confinement of the incident field at the tips leading to a stronger multipolar emission from nanostars. As shown in Appendix B, nanostars susceptibilities magnitudes can be much higher than in KTP when one takes into account the volume of excitation of the nonlinear material. Near resonance, the susceptibilities also increase importantly.

Unlike molecules, gold nanoparticles are not subject to bleaching even under resonant excitation conditions, and photo-damage is most likely to occur from pure thermal effects. Taking into consideration that thermal effects can be minimized under adequate short pulse excitation conditions, we can argue that the use of gold nanoparticles benefits from more robust conditions, together with high signal to noise ratios.

Optics EXPRESS

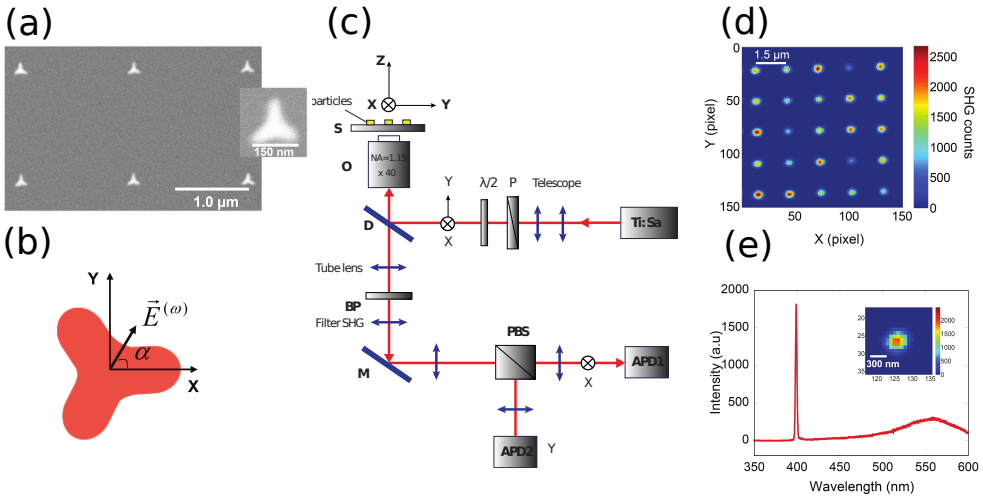


Fig. 1. (a) Scanning Electron Microscopy (SEM) images of nanostars. The metallic nanoparticles have been lithographed far enough from each other with the purpose of studying them independently. (b) Geometry used for positioning the nanoparticles in the sample plane (X,Y) for polarization resolved and efficiency measurements. (c) Schematic of the polarization resolved SHG experiment. (d) SHG scanning image of an array of nanostars. The scale represents the sum of the SHG signals over 32 incident polarization angles, in counts/100 $\mu$s, pixel size: 60 nm. (e) Emission spectrum from a single nanostar. Integration time: 1s.

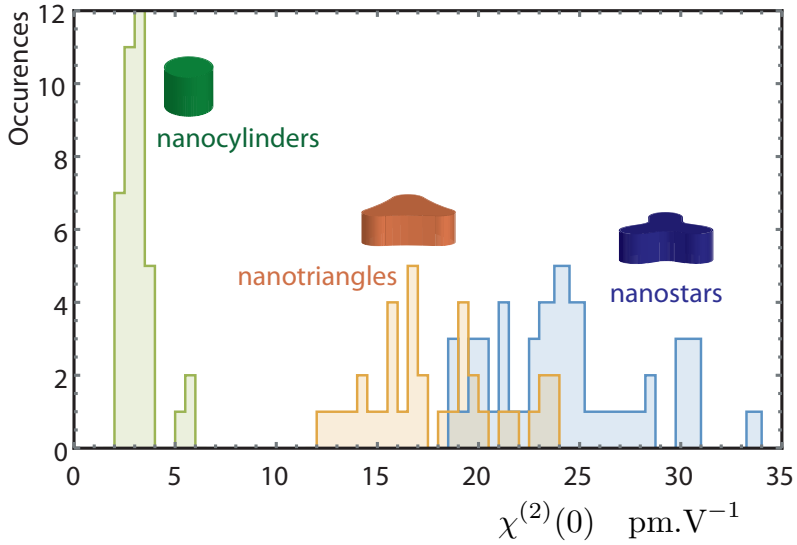


Fig. 2. Histograms of the off-resonant $\chi^{(2)}$ for nanocylinders, nanotriangles and nanostars, obtained by comparison with a bulk KTP crystal measurement (see Appendix B). 45 particles were measured for each shape.

The important difference in the SHG intensity of nanostars, nanotriangles and nanocylinders shows that the shape of the object is a crucial parameter: the factors that explain the high nonlinear

Optics EXPRESS

efficiency of threefold symmetry nanoparticles embed both symmetry and spatial extent effects. In the next section, a model describing those nonlinear responses and taking into account the shape variations is developed.

## 3. Modeling the nonlinear response of stars

In previous work on similar structures [28], we showed from numerical Finite Difference Time Domain calculations that, under linearly polarized excitation, a local confinement of the field scattered by branched particles occurs at their tips. This confined field was, moreover, strongly polarized along the tip direction, supporting the choice of linear induced dipoles along it.

We model the polarization resolved responses of nanostars by locating their induced nonlinear dipole sources close to the star tips. Three nonlinear sources, linked to the incoming field via the susceptibility tensors $\boldsymbol{\beta}_1$, $\boldsymbol{\beta}_2$, $\boldsymbol{\beta}_3$, are positioned at a distance $h$ from the center of the particle (Fig. 3). The hyperpolarizability $\boldsymbol{\beta}_i$ tensors exhibit three independent tensorial components [3,29]: $\boldsymbol{\beta}_{\uparrow\uparrow\uparrow}$, $\boldsymbol{\beta}_{\uparrow\perp\perp}$ and $\boldsymbol{\beta}_{\perp\uparrow\perp}$ where the symbol $\uparrow$ denotes the direction parallel to the tip of the star and $\perp$ is its perpendicular direction within the plane of the particle. With both theory and experiment, W. Hübner *et al* [30,31] showed that the tensorial element $\boldsymbol{\beta}_{\uparrow\uparrow\uparrow}$ dominates over the elements $\boldsymbol{\beta}_{\perp\uparrow\perp}$ and $\boldsymbol{\beta}_{\uparrow\perp\perp}$. We therefore consider as a first approximation that each induced dipole thus possesses one single tensorial coefficient $\boldsymbol{\beta}_{\uparrow\uparrow\uparrow}$ along each arm direction. Within this model, the nonlinear polarization at the tip $j$ is given by:

$$\boldsymbol{\mu}_{j\uparrow} = \varepsilon_0 \beta_{\uparrow\uparrow\uparrow} \cdot (\boldsymbol{E}^{(\omega)} \cdot \boldsymbol{e}_{j\uparrow}) \cdot (\boldsymbol{E}^{\omega} \cdot \boldsymbol{e}_{j\uparrow}) \cdot \boldsymbol{e}_{j\uparrow} \tag{1}$$

where $\boldsymbol{e}_{j\uparrow}$ is the unit vector parallel to the tip $j$ and $\boldsymbol{E}^{(\omega)}$ is the incoming electric field. With this model, the field enhancement due to the resonance of the nanoparticle would give a scalar modification of each multipole (the symmetry of the field is only affected by the symmetry of the nanoparticle): this does not affect the model. The radiation of the three induced dipoles is collected by a collection objective giving rise to three fields in the image plane (Fig. 3).

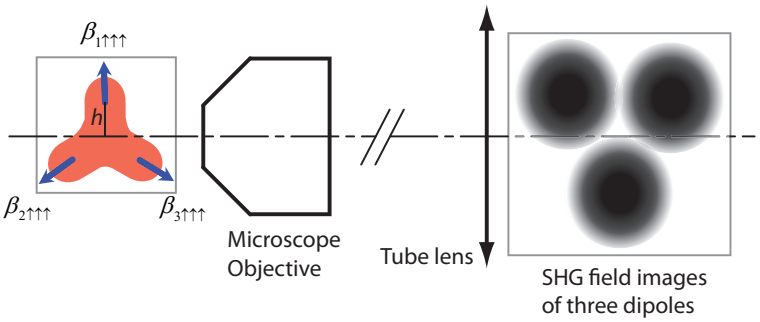


Fig. 3. The radiation of three SH induced dipoles through the collection objective of microscope giving rise to the three SHG field images.

The total SHG signal, collected by the detector in the image focal plane of the microscope, is given by independent contributions when the dipoles separation is large enough such that their images do not overlap (see Appendix C).

We use exact forms of the imaged electric fields to calculate the total detected signal on the detector (see Appendix D). The imaged field of a radiating dipole through an aplanetic optical objective is known [32–35] and these expressions are used to calculate the signal. An overlap parameter $c$ is introduced to weigh the importance of this overlap (see Appendix E). This overlap parameter can be expressed as a function of the distance $h$ separating the three dipoles from the center of the star. $c$ also depends on the parameters of the optical microscope, the magnification

Optics EXPRESS

$M$ and the numerical aperture $NA = n \sin\theta_m$ ($\theta_m$ is the half-aperture angle):

$$c = \frac{4}{\pi} \int_0^1 \frac{\sin(\sqrt{3}\, M\, a\, h\, \sqrt{1-v^2})}{\sqrt{3}\, M\, a\, h}\, dv \tag{2}$$

with $a = \frac{k\theta_m}{M}$ and $k$ is the wavevector of the nonlinear emission in the medium used for imaging.

The total SHG signal $s_{\text{total}}$, defined as the total intensity integrated over the photodetector surface, is found experimentally to be independent of the polarization of the exciting field. The model developed here shows it too, extending the evidence for the linear response in previous studies [36]. In order to quantitatively determine $c$ from experimental data, we have used a polarization beam splitter to measure signals projected along the $X$ ($s_x$) and $Y$ ($s_y$) axes of the sample plane. These contributions to the signal are plotted in Fig. 4 as a function of the polarization of $\boldsymbol{E}^{\omega}(\alpha)$, $\alpha$ being defined as the angle between $X$ and $\boldsymbol{E}^{\omega}$. The polarization-resolved signals vary strongly with the $c$ parameter. When $h$ is close to 0 (three dipoles located at the center, Fig. 3(a)), radiations fully overlap and the resulting polarization dependence exhibit characteristic lobes of symmetric threefold structures in the dipolar approximation [37]. When $h$ increases (Figs. 4(b)–4(f)), the overlap of the three dipolar images decreases and spatial phase delay effects intervene in the signal build-up. The signal thus contains partial spatial incoherent contributions and, consequently, an opening of the lobes appears. When the dipolar images do not overlap, the signal loses its sensitivity to the nanostructure threefold symmetry. SHG polarization responses are therefore highly informative about both the symmetry, the size and the shape of the nanoparticles.

## 4. Discussion

### 4.1. Comparison of modeling with experimental results

Experimental SHG polarization responses were recorded for a large quantity of single nano-stars. The polarization responses show deviations from particle to particle. About half of the whole investigated population exhibit a pure four lobes polarization dependence for both $s_X(\alpha)$ and $s_Y(\alpha)$, whereas the rest of the population exhibit just two lobes. The SEM images corresponding to the measured particles were also investigated, and show various shapes deformations. A careful check of the SEM images of recorded particles before and after SHG measurement shows that shape deviations occur only during the fabrication processes, i. e. the SHG measurement does not damage the particles. Comparing each shape of the nanoparticles and its SHG polar response, we observe that when a particle loses its threefold symmetry, even with a slight deviation, its polarization response exhibits a shape with two lobes. On the other hand, the particles possessing a four lobes polar responses are the one whose geometry is not deformed from the ideal three-branched star shape.

The symmetry of a nanostar can be lost in multiple ways: difference in arm length or angular deformations. The model developed in the previous section is therefore not sufficient to describe the variety of imperfections and we introduce a second model, defined in Fig. 5: three different dipoles of strengths $\beta_1$, $\beta_2$ and $\beta_3$ with angles $\nu_1$ and $\nu_2$ between the dipoles are considered. Moreover, an angle $\varphi$ is included to describe an overall rotation of the object in the (X,Y) plane (see Fig. 5(a)). The $\varphi$ angle thus describes the orientation of a given nanoparticle in the laboratory frame while the $\alpha$ angle indicates the direction of the incoming field polarization.

Fitting results show a good agreement between the second model and the experimental data. The fitting of both $s_X(\alpha)$ and $s_Y(\alpha)$ were performed at the same time, using the same fitting parameters as described in the models above. Note that the use of two polarizations allows the determination of 8 independent parameters, which is consistent with the choice of the unknown fitting parameters in the models. The fitting parameters show that four lobes angular patterns are obtained when the threefold symmetry is present (allowing slight angular deviation).

Optics EXPRESS

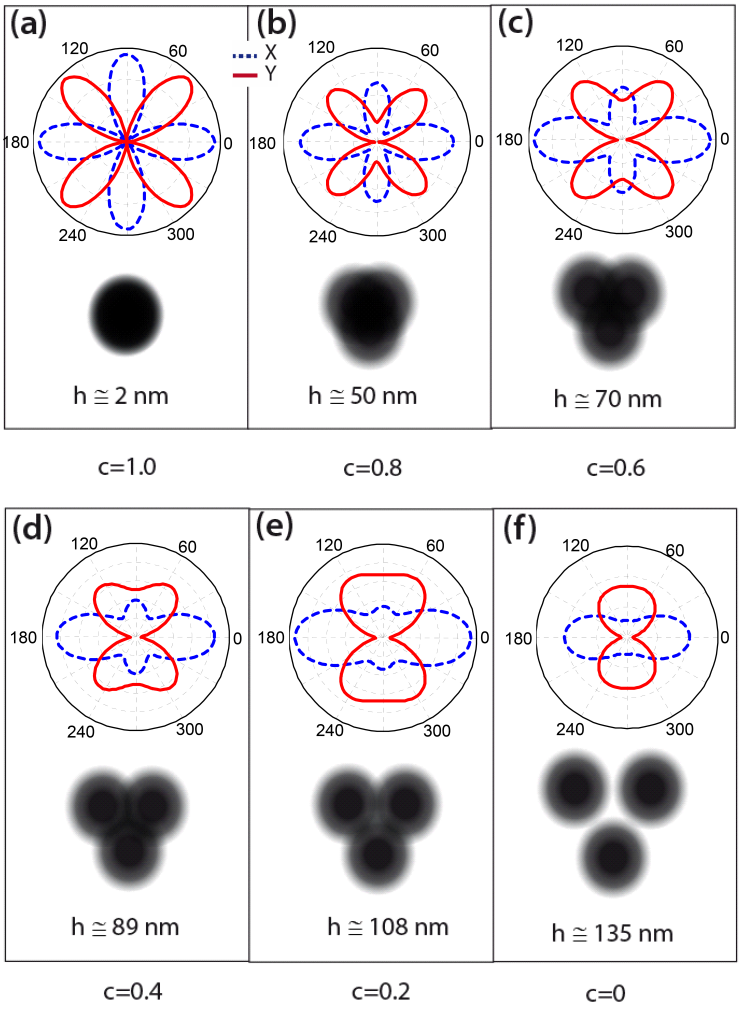


Fig. 4. SHG signals as a function of the polarization angle along the X and Y axes ($s_X$ in blue and $s_Y$ in red) with various values of $c$ corresponding to the distance h from the center of star to the position where the SH induced dipole sources located. Two lobes polar patterns are a signature of non-overlapping signals whereas four lobes ones denote fully overlapping signals, typical of a threefold symmetry [37].

Comparison with the SEM images (Fig. 5) confirms this observation. The threefold symmetry of the nonlinear induced dipoles is slightly modified for nanoparticles deviating from a perfect shape. Figure 5(b) shows an example of a nanostar which SEM image exhibit a clear deviation from the threefold symmetry. The SHG polarized responses can be explained by tips of different nonlinear efficiencies as well as orientation. In this example, the nanostar loses its threefold symmetry since one arm is visibly larger than the two other ones.

The strength of the dipoles efficiencies $\beta_1$, $\beta_2$ and $\beta_3$ are related to the confinement of the linear excitation field in the structure (governed by both tip arm and tip end shape), while their orientation is clearly related to the symmetry of the nanoparticle. Angular patterns from triangle-shaped nanoparticles can also be fitted with our three-dipoles models, supporting the fact that the symmetry of the structure is strongly affecting the SHG polarized response.

Optics EXPRESS

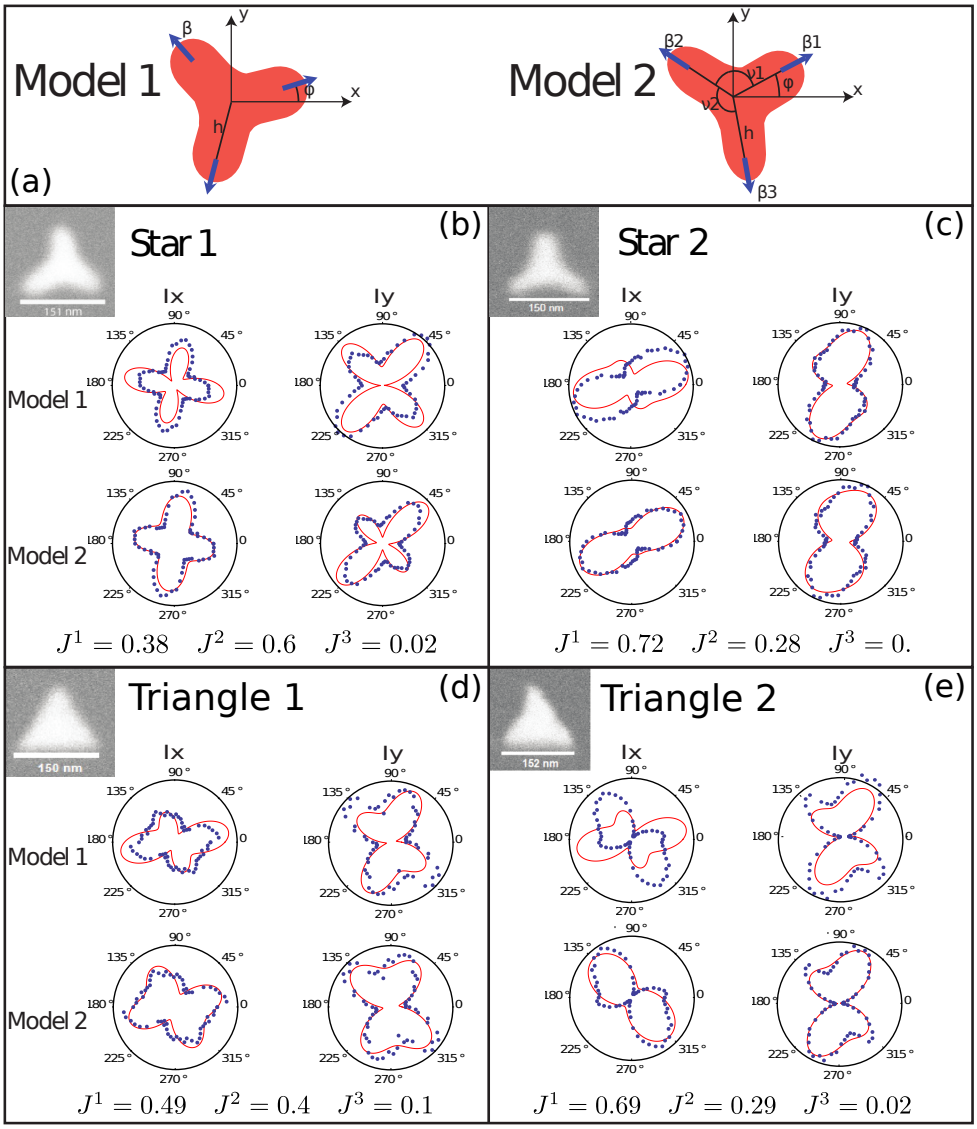


Fig. 5. (a) Schematic of the two fitting models. Model 1: Three dipoles of strength $\beta$ located at a distance $h$ from the center and separated by $\frac{2\pi}{3}$. Model 2: Three dipoles of different strengths $\beta_1, \beta_2$ and $\beta_3$ and arbitrary angles $\nu_1$ and $\nu_2$. Fitting results obtained on the data of two typical nanostars (b), (c) and two typical triangles (d), (e). Particle (b) and (d) have an almost perfect threefold symmetry while (c) and (e) are deformed. Fitting parameters from the models are given in Appendix, table 2.

### 4.2. *Direct symmetry read-out: introducing multipolar description*

The experimental results obtained on nanostars and nanotriangles are properly fitted using the model of the previous section. This model has permitted us to understand the high sensitivity of the response to the shape of the nanoparticle. This possibility to tune the polar response of a nonlinear emitter thanks to its shape is new compared to previous works on octupolar molecules and offers new engineering possibilities. For example, the insensitivity of the polar response is strongly due to the symmetry of the object [28]. This is a non-trivial property which depends on

Optics EXPRESS

the nonlinear order of the interaction with the nanoparticle.

However, even if this model respects the symmetry of the nanoparticle, it does not highlight the influence of the geometry of the object since it is not treated as a whole but as a collection of dipoles. In particular, subtle differences between triangles and nanostars are not necessarily visible from such analysis. Moreover, it is possible to describe in principle any kind of particle shape by choosing an appropriate set of dipoles distribution, but this choice would not make the physical interpretation much clearer. It is then interesting to treat the object as a whole with a unique response tensor which would include the full symmetry of the nanoparticle directly.

For punctual objects, expansion of the hyperpolarizability in irreducible parts [38] has shown that the high nonlinear efficiency of molecules was due to an important octupolar tensor part. Although multipolar elements play an important role in the nonlinear response, radiations from these molecules are still purely dipolar. However, a nanoparticle is an extended object and the richness of its physics is due to its spatial extension and shape. Therefore, one cannot just simply use a local irreducible formalism to describe its nonlinear response. It can be shown that, as the size of the nanoparticle increases, higher multipolar radiations appear. To quantify those radiations, the radiated electric field needs to be projected on the basis of electric and magnetic vector spherical harmonics [39] which are defined in the following way (in spherical coordinates):

$$\boldsymbol{\Psi}_m^{JM}(r,\theta,\varphi) = \frac{1}{\sqrt{J(J+1)}} j_J(kr)\boldsymbol{L}Y_{JM}(\theta,\varphi) \tag{3}$$

$$\boldsymbol{\Psi}_e^{JM}(r,\theta,\varphi) = \frac{i}{k}\nabla \wedge \boldsymbol{\Psi}_m^{JM}(r,\theta,\varphi) \tag{4}$$

Where $Y_{JM}$ are the scalar spherical harmonics, $\boldsymbol{L} = \frac{1}{i}(\boldsymbol{r} \wedge \nabla)$ is the orbital angular momentum operator and $j_J$ is the spherical Bessel function of order $J$. This set of functions constitutes a basis for radiation from any source of the Helmholtz equation. The first order $J = 1$ corresponds to the usual electric and magnetic dipolar radiations and the higher orders are the quadrupolar ($J = 2$) and octupolar ($J = 3$) orders. It should be noted that in this formalism, in contrast with the previous section, this dipolar radiation is the rigorous one in electrodynamics which should not be mistaken with a doublet radiation. The former one is always strictly a dipole while the latter has higher multipolar components in near-field.

To explicitly express the impact of symmetry on the measured SHG signals, we define the multipolar coefficients that are obtained by a direct projection of the current distribution in the following way:

$$J_i^{JM}(c) = \int \boldsymbol{J}(c,r) \cdot \boldsymbol{\Psi}_i^{JM} dV \tag{5}$$

Where $i$ refers to $m$ or $e$ and $\boldsymbol{J}(c,r)$ is the current distribution generated by the three punctual dipoles according to the model of section 3. The norm of an irreducible tensor $T^J$ is defined as [40] $\sum_M (-1)^M T^{JM} T^{J-M}$. Then, the norm of the coefficients over a whole subspace is calculated and normalized in order the measure the relative multipolar contributions.

$$J^J(c) = \frac{\sum_{iM}(-1)^M J_i^{JM}(c) J_i^{J-M}(c)}{\sum_{JiM}(-1)^M J_i^{JM}(c) J_i^{J-M}(c)} \tag{6}$$

Table 1 shows that, in the perfect threefold symmetry model, the radiation has to be described using more and more multipolar orders as the size of the nanoparticle described by the increases. Indeed, when the particle has no spatial extension ($h = 0$) only a dipolar radiation is emitted as it is observed in the molecular case. Moreover, for the size of the nanoparticle considered, only three orders of the multipolar expansion are necessary since the $J = 4$-pole does not appear for small nanoparticles. By comparing SEM images, SHG efficiencies and polarization resolved

Optics EXPRESS

Table 1. Relative weights of the different multipole orders for various values of the nanostar size $h$. The model depends on three identical dipoles oriented in a threefold symmetry structure and a variable distance from the nano-star center.

| Multipolar orders $J^J(c)$ | Dipole | Quadrupole | $J$ = 3-pole | $J$ = 4-pole |
|---|---|---|---|---|
| $c = 1$ ($h = 0$) | 1 | 0 | 0 | 0 |
| $c = 0.8$ ($h = 50$ nm) | 0.81 | 0.18 | 0.01 | 0. |
| $c = 0.6$ ($h = 70$ nm) | 0.66 | 0.30 | 0.04 | 0. |
| $c = 0.4$ ($h = 89$ nm) | 0.52 | 0.40 | 0.08 | 0. |
| $c = 0.2$ ($h = 108$ nm) | 0.39 | 0.47 | 0.14 | 0.01 |

responses, we observe that particles with a high nonlinear efficiency and an almost perfect threefold symmetry are also the ones displaying a multipolar radiation pattern.

Multipolar contributions obtained for nanotriangles and nanostars from experimental data and for all models are given in the Appendix F for the two models presented here. The first model which considers three equivalent dipoles separated by $\frac{2\pi}{3}$ has been useful to describe an ideal star but does not provide excellent fits on the real nanostars. This is due to the deformation of the nanostars and then, a second model has been proposed to improve it by allowing the dipoles to be oriented freely. It gives a better fit and then the polar responses are sensitive to deviation in the orientation of the dipoles. The multipolar distribution becomes dependent on the angle $\alpha$ of the incoming field polarization. In Fig. 5, we provide the multipolar weights for four nanoparticles using the imperfect nanoparticle model at the angle that maximize the quadrupolar contribution. This is done by projecting the three dipoles obtained by the data fitting onto the basis of electric and magnetic vector spherical harmonics at the nanoparticle center and then by taking the norm defined in Eq. (6). We observe that triangles always have a dominant dipole contribution to their radiation, explained by a stronger deviation from an optimal multipolar structure. One can observe that the star 1 possesses a much more important quadrupolar part than the star 2. On the other side, the multipolar distribution of triangles is quite robust to shape deformation although they do not have a great SHG efficiency.

In triangles, the emitting dipoles effective locations are closer to the center of the particle center and generate mainly dipole radiation. The sum of multiple dipoles on top of each other gives in general dipole radiation. In contrast, nanostars having an almost perfect symmetric threefold shape have a dominant quadrupolar contribution (the asymmetry of the real star creates a non-constant polar response). However, nanostars that deviate strongly from the ideal shape do not have this property and the dipolar contribution becomes dominant.

## 5. Conclusion

Nonlinear plasmonics is a rather young field that offers the opportunity to design future nonlinear optical components with improved integration and ultrafast response [41]. However, a complete understanding of the link between overall geometry and nonlinear responses is still lacking. The multipolar analysis presented in this article provides a framework to fill this gap and to optimize nonlinear responses. The models presented here use a discrete set of radiating dipoles. Although correct when using enough dipoles [42], the multipolar nature of the problem suggests that a description of the radiation as a sum of multipole located at the origin of the nanoparticle would provide more physical insights.

Optics EXPRESS

Experimental data indicate that the high SHG efficiency of threefold nanostar is due to their strong quadrupolar radiations. This property is lost for nanotriangles or deformed nanostars that have optical properties dominated by their dipolar radiations. The nonlinear optical properties can be linked to the nanoparticles' shape through a rigorous multipolar framework. Further developments on the interplay between multipolar radiation and nonlinear optical responses can thus help to design nanoparticles with desired properties. Theoretical works [43] together with continuous technological progress [44] will help designing efficient nonlinear nano-emitters based on their multipolar properties as it was done for molecular crystal in the past.

## Appendix A: Experimental setup

Nanostars were fabricated on glass substrates by electron beam lithography and were imaged using a scanning electron microscope (SEM) [45] as can be seen in Fig. 1 in the main text. $5 \times 5$ square patterns of 6 $\mu$m $\times$ 6 $\mu$m size with inter-pattern distance of 18 $\mu$m were prepared, in which a single pattern consists of $5 \times 5$ gold particles with an inter-particle distance of 1.5 $\mu$m in two perpendicular directions, allowing to investigate them individually. Nanotriangles (150 nm of edge length and 50 nm thickness) and nanocylinders (130 nm diameter and 60 nm thickness) were also prepared to compare the SHG efficiencies.

Nonlinear optical measurements of nanostars were carried out by an inverted two-photon excitation microscope [46] represented in Fig. 1(c) in the main text. A mode locked Ti: Sa produces 150 fs pulses at a fundamental wavelength of 800 nm with a 80 MHz repetition rate. The laser beam is focused on the sample by a high numerical aperture water immersion objective (×40, NA=1.15), leading to a lateral optical resolution of about 300 nm. The SHG emitted by the sample is collected by the same objective, spectrally filtered around the second harmonic wavelength (400 nm) by visible band pass and interference filters. The signal is then directed to a set of two photo-multipliers of large size, working in the photon counting mode, along two perpendicular polarization directions by means of a polarizing beam splitter. The collected SHG signals are denoted $s_X$ and $s_Y$. The polarization analysis is done by rotating the incident fundamental polarization in (X,Y) sample plane while measuring the optical SHG responses in the two X and Y directions. One image was recorded for each linear incident polarization angle $\alpha$, varied between 0° and 180° relative to the X horizontal sample direction, in 32 steps. Collection over the full 360° has not been carried out in order to minimize damages on the nanoparticles. This method permits to obtain a collection of images corresponding to multiples angles of the incident linear polarization. Typically, an image of the $9 \times 9$ $\mu$m$^2$ sample (5×5 particles) takes less than one minute of acquisition. The image size is $150 \times 150$ pixels and the dwell time per pixel is around 100 $\mu$s. The polarimetric SHG responses for each single particle of this array are then plotted on polar graphs by averaging the $s_X(\alpha)$ and $s_Y(\alpha)$ signals on an area of 10×10 pixels around the center of the nanoparticle.

Figure 1(d) in the main text depicts the image that is retrieved from the total signal $s_X(\alpha)$ + $s_Y(\alpha)$ summed over the 32 incident polarization angles $\alpha$ as defined in Fig. 1(b) in the main text. The particles are identified by bright diffraction-limited spots. The panel (e) shows a typical two-photon excited emission spectrum of a single nano-star placed at the center of the focal spot and directing its emission to a spectrometer at the exit of the microscope. The emission spectrum shows a very strong SHG emission at 400 nm, sufficiently well separated from the two-photon luminescence of the nanoparticle centered at 550 nm.

## Appendix B: Nonlinear coefficients estimation from a bulk KTP comparison

We analyze the SHG efficiency of the nanoparticle by comparing it to a reference Potassium-Titanyl-Phosphate (KTP) crystal. KTP has a nonlinear $\chi^{(2)}_{333}$=34 pm/V along its 3-labeled unit cell direction in off-resonance conditions [47].

Optics EXPRESS

The final expression for the SHG intensity induced by an incident field $E^{(\omega)}$ field can be expressed as

$$I^{(2\omega)} = C.(V_{\text{exc}})^2.(\chi^{(2)})^2.(I^{(\omega)})^2 \tag{7}$$

Where $C$ is an experimental constant containing collection efficiencies and $I^{(\omega)}$ is the incident intensity in the excitation volume.

We write Eq. (7) for nano KTP as

$$I^{(2\omega)}_{\text{KTP}} = C.(V_{\text{exc-KTP}})^2.(\chi^{(2)}_{\text{KTP}})^2.(I^{(\omega)}_{\text{KTP}})^2 \tag{8}$$

In the present experiment, the Y axis of the macroscopic coordinates is set along the KTP axis "3". Since $\chi^{(2)}_{333}$ is much larger that the other components of the KTP susceptibility [48], we can approximately consider that $\chi^{(2)}_{\text{KTP}} \approx \chi^{(2)}_{YYY}$.

Because the nanoparticles volume is smaller than the excitation volume, the measured SHG is created by a fraction of the energy of the incoming field. Thus, to make the comparison possible with a KTP crystal (that can use the full excitation volume), we take into account that only a fraction of the energy of the incoming field is used in nanoparticles, this fraction being proportional to the ratio between the excitation volume and the volume of the nanoparticle. Thus, the SHG intensity (sum of average intensities collected in X and Y directions) is given by:

$$I^{(2\omega)}_{\text{particle}} = C.(V_{\text{exc-particle}})^2.(\chi^{(2)}_{\text{particle}})^2.(I^{(\omega)}_{\text{particle}})^2 \tag{9}$$

From Eqs. (8) and (9), we deduce the value of second order susceptibility of nanoparticle

$$\chi^{(2)}_{\text{particle}} = \chi^{(2)}_{YYY,\text{KTP}} \cdot \sqrt{\frac{I^{(2\omega)}_{\text{particle}}}{I^{(2\omega)}_{\text{KTP}}} \cdot \frac{I^{(\omega)}_{\text{particle}}}{I^{(\omega)}_{\text{KTP}}} \cdot \frac{V_{\text{exc-KTP}}}{V_{\text{exc-particle}}}} \tag{10}$$

In practice, $I^{(\omega)}_{\text{KTP}}$ and $I^{(\omega)}_{\text{particle}}$ are the measured SHG photons counts for an incident polarization along Y, and along the detector analyzing the emission in the Y direction. Results for nanocylinders, nanotriangles and nanostars are given in Fig. 6.

According to the previous discussion, our experimental setup gives the following values for the excitation volume and KTP excited volume:

- Nanoparticles' lateral sizes are smaller than the illumination spot size. Particles do not probe the whole cross section of the excitation laser beam in the sample plane as in the case of KTP crystal. In the lateral dimension, the nanoparticles surface is 10 000 nm$^2$ whereas, in KTP, the excitation occurs over the whole surface, that is 70 000 nm$^2$ (the diameter of the nonlinear excitation point spread function is about 300 nm).

- In the transverse direction, the phase matching conditions occurring in the backward detection direction are considered. The particles emit SHG from their whole volumes and radiate coherent SHG over their 50 nm heights. The KTP crystal, excited over the whole point spread function length (about 700 nm), will undergo coherent build up conditions which will limit the interaction length at the crystal surface to the coherence length of the backward SHG emission process. The calculation of this coherence length for the 800 nm / 400 nm conversion process uses the backward phase matching wave vector difference [49]:

$$\triangle k = 2k_\omega + k_{2\omega} = 2\frac{2\pi}{\lambda}(n_\omega + n_{2\omega}) \quad \text{and} \quad \frac{\triangle k\, l_{\text{coherent}}}{2} = \frac{\pi}{2} \tag{11}$$

(with $\lambda = 800nm$, $n_\omega = 1.84465$, $n_{2\omega} = 1.93828$ [50]. This leads to a coherence length of 53 nm. Considering that the SHG coherent build up takes place over a 53 nm length, this leads to an interaction volume $V_{exc-KTP}$ of diameter 300 nm and height 53 nm.

Optics EXPRESS

Table 2. Parameters describing the susceptibilities of nanostars, nano triangle and nanocylinders obtained from experimental fits.

| Parameters | $\lambda_{max}$ | $M(\Omega)$ | $\gamma$ (Hz) |
|---|---|---|---|
| nanostar | 800 nm | 12.8 | $1.85 \times 10^{14}$ |
| nanotriangle | 800 nm | 11.8 | $2.02 \times 10^{14}$ |
| nanocylinder | 640 nm | 6.2 | $4.69 \times 10^{14}$ |

Fitting the extinction spectra with Lorentzian as discussed in the main text gives the parameters in table 2 to describe the resonant behavior of the nonlinear susceptibility.

Figure 7(a) shows the histogram of the obtained second order susceptibility $\chi^{(2)}$ deduced from the SHG intensities measured along the Y axis (as defined in Fig. 1(b) of the main text) for isolated particles corresponding to the direction of a branch. The $\chi^{(2)}$ values are determined following the methodology presented here, and using bulk KTP crystal as a reference value (34pm/V).

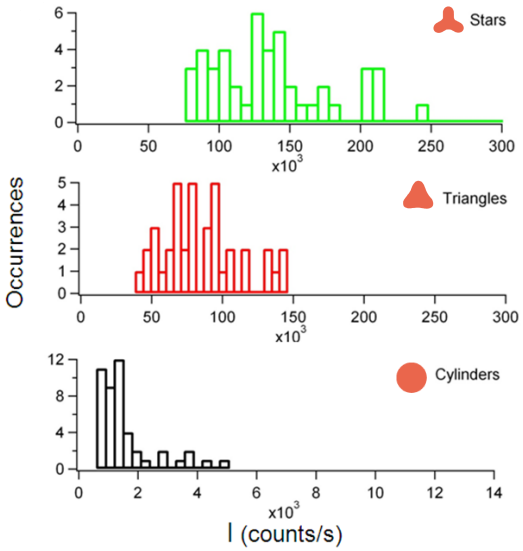


Fig. 6. Histogram of intensities collected from a population of 45 individual nanostars (top), nanotriangles (middle), and nanocylinders (bottom), with an incident averaged power of 0.4 mW at the focal spot of the objective. The obtained average and standard deviation values are: (140 090 ± 52 200) counts/s (nanostars), (84 800 ± 27 800) counts/s (nanotriangles), (1 520 ± 1 040) counts/s (nanocylinders).

After wavelength dependence correction, the off-resonant $\chi^{(2)}(0)$ value is seen to be roughly an order of magnitude lower than the one obtained by excitation at 800 nm (Fig. 7(a)).

Optics EXPRESS

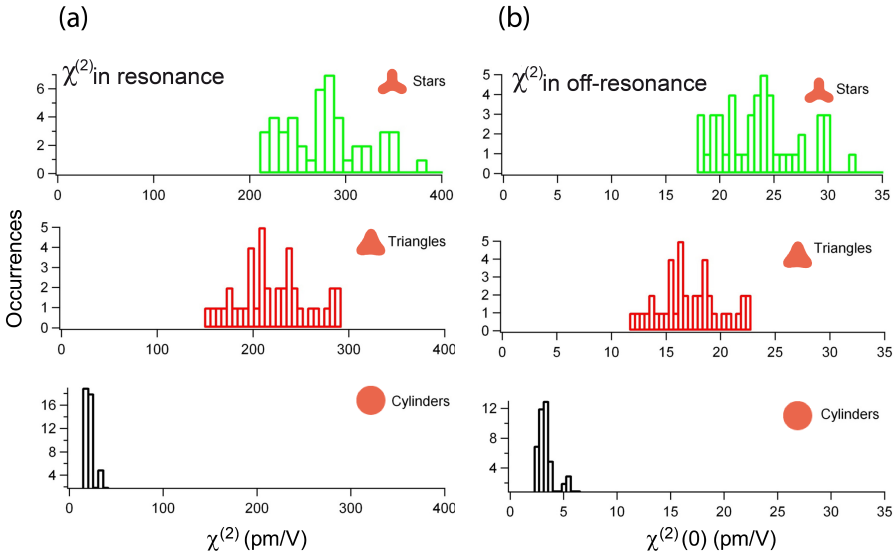


Fig. 7. (a) Histogram of the nonlinear coefficients $\chi^{(2)}$ obtained by comparison with a bulk KTP crystal measurement (see text). (b) Histogram of $\chi^{(2)}$ values corrected from the resonance to non-resonance factors obtained for the nanoparticles.

## Appendix C: Dipole imaging through an optical system

The electric field at a point $\vec{r}$ of an arbitrarily oriented electric dipole located at $\vec{r}_n$ with dipole moment $\vec{\mu}$ is defined by the dyadic Green's function $\mathbf{G}_{PSF}(\vec{r})$ as [33, 35]:

$$\vec{E}(\vec{r}) = \frac{\omega^2}{\varepsilon_0\, c^2}\, \mathbf{G}(\vec{r}, \vec{r}_n) \bullet \vec{\mu} \tag{12}$$

Where $\omega$ is the frequency of the incident light. We choose the dipole to be located at the origin (the focal point) $\vec{r}_n = \vec{0}$ and surrounded by a homogeneous medium of index $n_0$. The Green's function $\mathbf{G}_{PSF}$ expression is found in [33, 35]. In the imaging condition of this experiment, the Z component of the electric image field of a dipole is much smaller than the X and Y components. Then, by using the paraxial approximation, some tensorial elements of the PSF are neglected. Finally, the expression of dyadic Green's function $\mathbf{G}_{PSF}$ is:

$$\mathbf{G}_{PSF}(r) = K \begin{pmatrix} A_0(r) & 0 & 0 \\ 0 & A_0(r) & 0 \\ 0 & 0 & 0 \end{pmatrix} \tag{13}$$

$K$ is a constant characterizing the optical setup. The function $A_0(r)$ is given by:

$$A_0(r) = 2\, \frac{M\, \theta_m}{k\, r}\, \mathrm{J}_1\!\left(\frac{k\, r\, \theta_m}{M}\right) \tag{14}$$

Where $\mathrm{NA} = n_0 \sin\theta_m$ is the numerical aperture NA of the objective lens, $M$ is the magnification factor and $k = \dfrac{2\,\pi}{\lambda}$ is the wave vector.

If the dipole $\vec{\mu}$ is located in the focal plane at position $\vec{r}_n = (x_n, y_n, z_n)$, out of the focal point

Optics EXPRESS

of the objective lens, the electric field response of this dipole is:

$$\vec{E}(\vec{r} - M\,\vec{r}_n) = \frac{\omega^2}{\varepsilon_0\, c^2}\,[\,\mathbf{G}_{PSF}(\vec{r}) \bullet \vec{\mu}] * \delta(\vec{r} - M\,\vec{r}_n) \tag{15}$$

We assume that the induced nonlinear dipole sources are located near the tips of the nanostars. Each second harmonic dipole is treated as a point dipole with hyperpolarizability $\beta$. Each dipole is attached to one local coordinate in which $\vec{e}_\uparrow$ and $\vec{e}_\perp$ are the unit vectors parallel and perpendicular to the arm of the nanoparticle respectively. From Eq. (1) in the main text, the dipoles SHG polarization along the nanoparticles' arms is:

$$\mu_{j\uparrow}^{(2\omega)}(\alpha) = \varepsilon_0\, \beta_{j\uparrow\uparrow\uparrow}.\,[E_{j\uparrow}^{(\omega)}(\alpha)]^2 \tag{16}$$

The second harmonic response of each SH induced dipole in the image plane is:

$$\vec{E}_j^{(2\omega)}(\vec{r}) = \frac{\omega^2}{\varepsilon_0^2\, c^2}\,\left[\mathbf{G}(\vec{r}) \bullet \vec{\mu}_{j\uparrow}^{(2\omega)}\right] * \delta(\vec{r} - M\,\vec{r}_n) \tag{17}$$

The convolution operation is used to shift the signal from the center of the image plane to the position corresponding to the location of the dipole in focal plane. The amplitude of the signal does not change when a dipole is translated in the focal region. The imaged field for each SH induced dipole is:

$$\vec{E}_j^{(2\omega)}(r,\alpha) = K\,\frac{\omega^2}{\varepsilon_0^2\, c^2}\begin{pmatrix} A_0(r) & 0 & 0 \\ 0 & A_0(r) & 0 \\ 0 & 0 & 0 \end{pmatrix}\begin{pmatrix} \mu_{j\uparrow X}^{(2\omega)}(\alpha) \\ \mu_{j\uparrow Y}^{(2\omega)}(\alpha) \\ \mu_{j\uparrow Z}^{(2\omega)}(\alpha) \end{pmatrix} \tag{18}$$

$\mu_{j\uparrow X}^{(2\omega)}$ and $\mu_{j\uparrow Y}^{(2\omega)}$ are the X and Y components of SH induced dipole and j denotes the arms j (j = 1, 2, 3).

## Appendix D: SHG signal on the detector

In the experiment, we use two photomultipliers to record the second harmonic signal emitted by the nanostar. One detector is used to collect the signal in the X polarization direction while the other collects the Y polarization.

The expression of second harmonic field emitted by one of the dipoles is (hereafter, $p = X$ or $Y$):

$$E_{jp}^{(2\omega)}(r,\alpha) = K\,\frac{\omega^2}{\varepsilon_0^2\, c^2}\,A_0(r)\,\mu_{j\uparrow p}^{(2\omega)}(\alpha) \tag{19}$$

The total signal recorded by the detectors is the integral of the intensity of the imaged field taken over their surface $S_{\text{dect}}$ :

$$s_p = \iint_{S_{\text{dect}}} I_p\, ds = \iint_{S_{\text{dect}}} |\sum_j E_{jp}^{(2\omega)}(r,\alpha)|^2 ds \tag{20}$$

Hereafter, we consider that the surface of the detector is large enough to collect all the light focused in the image plane by the focal system.

**Signal from one dipole**

First, we consider the case with only one dipole located in the focal plane. We introduce a new function $g_1(r)$ that satisfies the following conditions:

$$I_{1p}(r) = g_{1p}^2(r)\; s_{1p} \quad \text{and} \quad \iint g_{1p}^2(r)\, ds = 1 \tag{21}$$

Optics EXPRESS

The function $g_1(r)$ expresses the relation between the second harmonic field and the second harmonic signal. The intensity of one dipole is:

$$I_{1p}(r) = (E_{1p}^{(2\omega)}(r,\alpha))^2 = K^2 \frac{\omega^4}{\varepsilon_0^4 c^4} A_0^2(r) \left(\mu_{1\uparrow p}^{(2\omega)}(\alpha)\right)^2 \tag{22}$$

and the integrated signal $s_{1p}$ for one dipole is:

$$s_{1p} = \iint_{S_{\text{dect}}} I_{1p}(r)\, ds = \iint \left(E_{1p}^{(2\omega)}(r,\alpha)\right)^2 ds = K^2 \frac{\omega^4}{\varepsilon_0^4 c^4} \left(\mu_{1\uparrow p}^{(2\omega)}(\alpha)\right)^2 \iint A_0^2(r)\, ds \tag{23}$$

Inserting Eqs. (22) and (23) into Eq. (21), we get:

$$g_{1p}(r) = \frac{A_0(r)}{\sqrt{\iint A_0^2(r)\, ds}} \Longrightarrow g_{1p}(r) = \frac{A_0(r)\, \mu_{1p}^{(2\omega)}(\alpha)}{\sqrt{s_{1p}}} \quad \text{and} \quad g_{1p}(r) = \frac{E_{1p}^{(2\omega)}}{\sqrt{s_{1p}}} \tag{24}$$

**Signal from two dipoles**

Next, we consider the case of two dipoles with a known interdistance between them. For a system consisting of more than 2 dipoles, the electric field overlaps can be deduced from each pair of two dipoles and thus reduces to this case. Inserting Eq. (19) into Eq. (20), one obtains the SHG signal coming from two dipoles as:

$$s_p = K^2 \frac{\omega^4}{\varepsilon_0^4 c^4} \iint \left(\mu_{1\uparrow p}^{(2\omega)}(\alpha)\, A_{01}(r) + \mu_{2\uparrow p}^{(2\omega)}(\alpha)\, A_{02}(r)\right)^2 ds \tag{25}$$

Another form of Eq. (24) as $A_{0j}(r) = \dfrac{\sqrt{s_{jp}}\, g_{j\uparrow p}(r)}{\mu_{j\uparrow p}^{(2\omega)}(\alpha)}$ is inserted into Eq. (25), then we get:

$$\begin{aligned} s_p &= \iint (s_{1p}\, g_{1p}^2(r) + s_{2p}\, g_{2p}^2(r) + 2\sqrt{s_{1p}}\sqrt{s_{2p}}\, g_{1p}(r)\, g_{2p}(r))\, ds \\ &= s_{1p} + s_{2p} + 2\sqrt{s_{1p}}\sqrt{s_{2p}} \iint g_{1p}(r)\, g_{2p}(r)\, ds \\ &= \left(1 - \iint g_{1p}(r)\, g_{2p}(r)\, ds\right)(s_{1p} + s_{2p}) + \left(\iint g_{1p}(r)\, g_{2p}(r)\, ds\right)(\sqrt{s_{1p}} + \sqrt{s_{2p}})^2 \end{aligned} \tag{26}$$

- When $\iint g_{1p}(r)\, g_{2p}(r)\, ds = 0$, the total signal coming from two non-overlapping dipoles given in Eq. (26) becomes the incoherent sum of their intensities $s_p = s_{1p} + s_{2p}$

  The signal characterizing this case is described in Fig. 8(a). The two PSF do not overlap when the dipoles are far enough from each other. This distance will be calculated in detail in the next subsection. The signals from each dipole add up in the definition of the total signal in an "incoherent" fashion. In the following, we name this signal as $\mathbf{s_{nov}}$ (no overlap signal).

- When $\iint g_{1p}(r)\, g_{2p}(r)\, ds = 1$, the total signal coming from two dipoles given in Eq. (26) becomes $s_p = (\sqrt{s_{1p}} + \sqrt{s_{2p}})^2$.

  Figure 8(c) shows the overlapping property of the two signals. When the dipoles are on top of each other, this signal is given by squaring the sum of electric response and is the fully overlapping signal $\mathbf{s_{fov}}$ (full overlap signal).

Optics EXPRESS

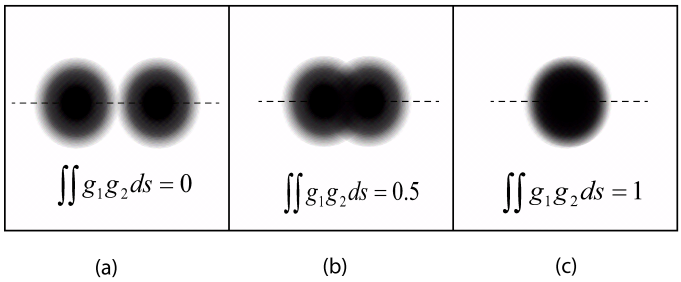


Fig. 8. Schematic of the overlap of the point spread function (PSF) for two dipoles: (a) $\iint g_1(r)\, g_2(r)\, ds = 0$, two PSF do not overlap. This case occurs when the distance between two dipoles is large. (b) $\iint g_1(r)\, g_2(r)\, ds = 0.5$, two PSF overlap partially and (c) $\iint g_1(r)\, g_2(r)\, ds = 1$, two PSF overlap fully. Case (c) occurs when two dipoles are located at the same position.

- $0 < \iint g_{ip}(r)\, g_{j\uparrow p}(r)\, ds < 1$

  Figure 8(b) illustrates the partial overlapping and the corresponding signal given by:

$$s_p = \left(1 - \iint g_{1p}(r)\, g_{2p}(r)\, ds\right) s_{nov-p} + \left(\iint g_{1p}(r)\, g_{2p}(r)\, ds\right) s_{fov-p} \tag{27}$$

The total signal is expressed as the sum of the fully overlapping and the non-overlapping signals. We introduce the parameter $c$ characterizing those contributions and defined by:

$$c = \iint g_{1p}(r)\, g_{2p}(r)\, ds = \frac{\iint A_{01}(r)\, A_{02}(r)\, ds}{\sqrt{\iint A_{01}^2(r)\, ds \iint A_{02}^2(r)\, ds}} \tag{28}$$

The Cauchy-Schwarz theorem gives the physically intuitive condition on $c$ : $0 \leq |c| \leq 1$.

**Signal from three dipoles (or more): nanostar case**

We now consider the case with three dipoles located in the focal plane of the objective lens. The signal coming from three dipoles is

$$s_p = \iint \Big(\sum_j \mu_{j\uparrow p}^{(2\omega)}(\alpha)\, A_{0j}(r)\Big)^2 ds = \sum_j s_{jp} + 2 \sum_{i,j} \sqrt{s_{ip}}\, \sqrt{s_{jp}} \iint g_{ip}(r)\, g_{jp}(r)\, ds \tag{29}$$

Where $i$ and $j$ indicate the dipole number and $i, j = 1, 2, 3$.

In the ideal case, the three tips have the same size and we can assume that $\iint g_i(r)\, g_j(r)\, ds$ does not depend on $i, j>$ The total signal of three dipoles given in Eq. (29) becomes:

$$s_p = \left(1 - \iint g_{ip}(r)\, g_{j\uparrow p}(r)\, ds\right) \sum_j s_{jp} + \left(\iint g_{ip}(r)\, g_{jp}\, ds\right) \Big(\sum_j \sqrt{s_{jp}}\Big)^2 \tag{30}$$

As in the two dipoles case, we analyze various limits of $\iint g_i(r)\, g_j(r)\, ds$ :

- When $\iint g_{ip}(r)\, g_{jp}(r)\, ds = 0$, the total SHG signal is given as the sum of intensities. The non-overlapping signal is: $s_{nov-p} = s_{1p} + s_{2p} + s_{3p}$.
- When $\iint g_{ip}(r)\, g_{jp}(r)\, ds = 1$, the fully-overlapping signal is $s_{fov-p} = (\sqrt{s_{1p}} + \sqrt{s_{2p}} + \sqrt{s_{3p}})^2$.

Optics EXPRESS

In the general case, $0 \leq \iint g_{ip}(r)\, g_{jp}(r)\, ds \leq 1$, the total SHG signal given Eq. (30) in terms of overlapping $s_{fov-p}$ and non-overlapping $s_{nov-p}$ contributions is:

$$s_p = \left(1 - \iint g_{ip}(r)\, g_{jp}(r)\, ds\right) s_{in-p} + \left(\iint g_{ip}(r)\, g_{jp}(r)\, ds\right) s_{co-p} \tag{31}$$

For the three dipoles case, the overlap parameter $c$ is defined as:

$$c_{ij} = \iint g_{ip}(r)\, g_{jp}(r)\, ds = \frac{\iint A_{0i}(r)\, A_{0j}(r)\, ds}{\sqrt{\iint A_{0i}^2(r)\, ds \iint A_{0j}^2(r)\, ds}} \tag{32}$$

If we consider that star is perfectly symmetrical, the $c_{ij}$ does not depend on the indices $i, j$ and $c_{ij} = c$.

- $c = 0$, the PSF of three dipoles do not overlap.
- $c = 1$, the PSF of three dipoles overlap completely.
- $0 < | c | < 1$ gives an intermediate behavior between the two previous cases.

## Appendix E: Calculation of the parameter $c$

In this section, we calculate the expression of the parameter $c$ and analyze how it weighs the contribution of the overlapping and non-overlapping signals.

As given in Eq. (32), the parameter $c$ is defined as:

$$c = \frac{\iint A_{0i}(r)\, A_{0j}(r)\, ds}{\sqrt{\iint A_{0i}^2(r)\, ds \iint A_{0j}^2(r)\, ds}} = \frac{\iint \frac{\mathrm{J}_1(a\, r)}{r} \frac{\mathrm{J}_1(a(r - r_0))}{r - r_0}\, ds}{\iint (\frac{\mathrm{J}_1(a\, r)}{r})^2\, ds} \tag{33}$$

Where, $a = \dfrac{k\, \theta_m}{M}$ and $r_0$ is the distance between the centers the two PSF.

We switch from cylindrical to Cartesian coordinates:

$$c = \frac{\iint \frac{\mathrm{J}_1\left(a \sqrt{x^2 + y^2}\right)}{\sqrt{x^2 + y^2}} \frac{\mathrm{J}_1\left(a \sqrt{(x - x_0)^2 + y^2}\right)}{\sqrt{(x - x_0)^2 + y^2}}\, ds}{\iint (\frac{\mathrm{J}_1\left(a \sqrt{x^2 + y^2}\right)}{\sqrt{x^2 + y^2}})^2\, ds} \tag{34}$$

The integrals $\left|\iint (\frac{\mathrm{J}_1\left(a \sqrt{x^2 + y^2}\right)}{\sqrt{x^2 + y^2}})^2\, ds\right|$ and $\iint \frac{\mathrm{J}_1\left(a \sqrt{x^2 + y^2}\right)}{\sqrt{x^2 + y^2}} \frac{\mathrm{J}_1\left(a \sqrt{(x - x_0)^2 + y^2}\right)}{\sqrt{(x - x_0)^2 + y^2}}\, ds$ are slowly converging due to their highly oscillatory variations and can be calculated in Fourier space using the Parseval-Plancherel theorem. The Fourier transform of the function $\dfrac{\mathrm{J}_1(r)}{r}$ is a constant function over a circular area and can be used on the Airy function:

$$\mathcal{F}\left(\frac{\mathrm{J}_1(a \sqrt{x^2 + y^2})}{\sqrt{x^2 + y^2}}\right) = \frac{2\,\pi}{a}\, \mathrm{circ}\left(\frac{2\,\pi}{a} \sqrt{\xi_x^2 + \xi_y^2}\right) \tag{35}$$

In addition, the Fourier transform of $\mathcal{F}\left(f\left(r - r_0\right)\right)$ is $e^{-2\,i\,\pi\,\mu\,r_0}\, \widetilde{f}(\mu)$. Combining with Eq. (35):

$$\mathcal{F}\left(\frac{\mathrm{J}_1(a \sqrt{(x - x_0)^2 + y^2})}{\sqrt{(x - x_0)^2 + y^2}}\right) = e^{-2\,i\,\pi\,x_0\,\xi_x}\, \frac{2\,\pi}{a}\, \mathrm{circ}\left(\frac{2\,\pi}{a} \sqrt{\xi_x^2 + \xi_y^2}\right) \tag{36}$$

Optics EXPRESS

By denoting $h(x_0)$ the numerator of Eq. (34), we write the $c$ parameter:

$$c = \frac{h(x_0)}{h(0)} \quad \text{with} \quad h(x_0) = \iint \frac{\mathrm{J}_1\left(a\sqrt{x^2+y^2}\right)}{\sqrt{x^2+y^2}} \frac{\mathrm{J}_1\left(a\sqrt{(x-x_0)^2+y^2}\right)}{\sqrt{(x-x_0)^2+y^2}}\, dx\, dy \tag{37}$$

By substituting Eqs. (35) and (36) into Eq. (37) and introducing $u = \frac{2\pi}{a}\xi_x$ and $v = \frac{2\pi}{a}\xi_y$,:

$$h(x_0) = \iint e^{-2i\pi x_0 \xi_x} \left(\frac{2\pi}{a}\right)^2 \mathrm{circ}^2\left(\frac{2\pi}{a}\sqrt{\xi_x^2+\xi_y^2}\right) d\xi_x\, d\xi_y = \iint e^{-2i\pi x_0 \frac{a}{2\pi} u}\, \mathrm{circ}^2\left(\sqrt{u^2+v^2}\right) du\, dv \tag{38}$$

Based on properties of circ function, we get:

$$h(x_0) = \int_{-1}^{1}\int_{-1}^{1} e^{-i a x_0 u}\, \mathrm{circ}\sqrt{u^2+v^2}\, du\, dv = 4\int_0^1 \frac{\sin\left(a x_0\sqrt{1-v^2}\right)}{a x_0}\, dv \tag{39}$$

For $h(0)$, we use $\lim_{x\to 0}\frac{\sin x}{x} = 1$, so $h(0) = 4\int_0^1 \sqrt{1-v^2}\, dv = \pi$. From Eqs. (39) and (37), we obtain the final expression of parameter c as

$$c = \frac{4}{\pi}\int_0^1 \frac{\sin\left(a x_0\sqrt{1-v^2}\right)}{a x_0}\, dv = \frac{4}{\pi}\int_0^1 \frac{\sin\left(a M d\sqrt{1-v^2}\right)}{a M d}\, dv$$

If we substitute $d = \sqrt{3}\, h$ into Eq. (40), we obtain the dependence of $c$ on the distance from the position of the induce SHG dipole to the center of particle as

$$c = \frac{4}{\pi}\int_0^1 \frac{\sin\left(\sqrt{3} M a h\sqrt{1-v^2}\right)}{\sqrt{3} M a h}\, dv \tag{40}$$

Its dependence on the translation length $h$ is represented in Fig. 9.

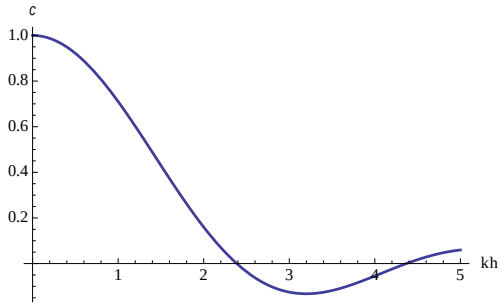


Fig. 9. Evolution of the overlap parameter $c$ as a function of the distance $h$ of translation of the dipole from the center of the star. When $h = 0$, the 3 dipoles are on top of each other and then interfere constructively. As $h$ increases, the overlap decreases and the dipoles start to interfere destructively.

## Appendix F: Fitting parameters for the models 1 and 2

Table 3 gives all the fitting parameters for the two models discussed in the main text computed on 4 typical nanoparticles, an almost perfect nanostars (star1), a slightly deformed one (star2) and the same for two nanotriangles (triangle1 and triangle2).

Optics EXPRESS

Table 3. This table summarizes the fitting parameters that have been calculated according to the two models given in the main text. Moreover, the right panel provides multipolar weight for each nanoparticles. These fits have been carried systematically for all nanoparticles and we provide here four typical cases. Stars (triangles) 1 and 2 refer to a perfect and a deformed nanostars (nanotriangles) respectively. For the model 2, the multipolar distribution is dependent on the angle $\alpha$ of the incoming field polarization and we thus give the multipolar weight for the stars for polarization that maximize the dipolar weight (noted *dip*) and the quadrupolar one (noted *quad*). The multipolar distribution of the triangle is quite robust to shape deformation and does not vary much with the polarization. For any case, $\beta_0 = 0$ and $\gamma = 0$.

| | Models | $kh$ | $\varphi$ | $\beta_1$ | $\beta_2$ | $\beta_3$ | $\nu_1$ | $\nu_2$ | $R^2$ | Dip. | Quad. | Octup. |
|---|---|---|---|---|---|---|---|---|---|---|---|---|
| Star 1 | M1 | 0.90 | 351 | 72.29 | 72.29 | 72.29 | 120 | 120 | 0.92 | 0.76 | 0.22 | 0.02 |
| | M2 *dip* | 0.90 | 351 | 80.76 | 80.99 | 79.98 | 145 | 92 | 0.96 | 0.82 | 0.17 | 0.01 |
| | M2 *quad* | " | " | " | " | " | " | " | " | 0.38 | 0.60 | 0.02 |
| Star 2 | M1 | 1.88 | 130 | 39.05 | 39.05 | 39.05 | 120 | 120 | 0.92 | 0.31 | 0.49 | 0.18 |
| | M2 *dip* | 0.01 | 122 | 758.4 | 47.60 | 762.7 | 93 | 85 | 0.98 | 1.00 | 0. | 0. |
| | M2 *quad* | " | " | " | " | " | " | " | " | 0.72 | 0.28 | 0. |
| Tri. 1 | M1 | 1.40 | 9 | 30.29 | 30.29 | 30.29 | 120 | 120 | 0.94 | 0.52 | 0.40 | 0.08 |
| | M2 | 1.63 | 14 | 25.96 | 33.89 | 28.67 | 117 | 117 | 0.98 | 0.49 | 0.40 | 0.10 |
| Tri. 2 | M1 | 1.49 | 311 | 41.72 | 41.72 | 41.72 | 120 | 120 | 0.85 | 0.48 | 0.43 | 0.10 |
| | M2 | 1.22 | 306 | 50.20 | 46.59 | 18.72 | 132 | 288 | 0.98 | 0.69 | 0.29 | 0.02 |

Model 1 refers to the "perfect threefold symmetry" case - three dipoles of equal strength oriented $2\pi/3$ from each other - while model 2 refers to the imperfect case involving dipoles of unequal weight and orientations. On the right side of the table, the norms of multipolar coefficients of the reconstructed emitted field from the fits are given for each nanoparticles and model. These norms are calculated using definitions given by expressions (5) and (6) in the main text.

## Funding

Agence Nationale de la Recherche (ANR) (JC07-195504); Conseil Régional de Provence-Alpes-Côte d'Azur; CNRS-Weizmann NaBi European associated laboratory; Conseil Régional de Champagne-Ardenne; Nano'MAT.

## Disclosures

The authors declare that there are no conflicts of interest related to this article.

## References

1. G. S. Agarwal and S. S. Jha, "Theory of second harmonic generation at a metal surface with surface plasmon excitation," Solid State Commun. **41**, 499–501 (1981).
2. N. Bloembergen, R. K. Chang, S. S. Jha, and C. H. Lee, "Optical second-harmonic generation in reflection from media with inversion symmetry," Phys. Rev. Lett. **174**, 813–822 (1968).
3. J. I. Dadap, J. Shan, and T. F. Heinz, "Theory of optical second-harmonic generation from a sphere of centrosymmetric material: small-particle limit," J. Opt. Soc. Am. B **21**, 1328–1347 (2004).
4. J. I. Dadap, J. Shan, K. B. Eisenthal, and T. F. Heinz, "Second harmonic Rayleigh scattering from a sphere of centrosymmetric material," Phys. Rev. Lett. **83**, 4045–4048 (1999).

Optics EXPRESS


5. S. D. Gennaro, M. Rahmani, V. Giannini, H. Aouani, T. P. Sidiropoulos, M. Navarro-Cía, S. A. Maier, and R. F. Oulton, "The interplay of symmetry and scattering phase in second harmonic generation from gold nanoantennas," Nano Lett. **16**, 5278–5285 (2016).
6. M. Finazzi, P. Biagioni, M. Celebrano, and L. Duo, "Selection rules for second-harmonic generation in nanoparticles," Phys. Rev. B **76**, 125414 (2007).
7. K. Frizyuk, I. Volkovskaya, D. Smirnova, A. Poddubny, and M. Petrov, "Second-harmonic generation in mie-resonant dielectric nanoparticles made of noncentrosymmetric materials," arXiv 1809.06456 (2018).
8. C. Hubert, L. Billot, P.-M. Adam, R. Bachelot, P. Royer, J. Grand, D. Gindre, K. D. Dorkenoo, and A. Fort, "Role of surface plasmon in second harmonic generation from gold nanorods," Appl. Phys. Lett. **90**, 181105 (2007).
9. G. Bachelier, I. R. Antoine, E. Benichou, C. Jonin, and P. F. Brevet, "Multipolar second-harmonic generation in noble metal nanoparticles," Phys. Rev. **25**, 955–960 (2008).
10. J. Nappa, I. R. Antoine, E. Benichou, C. Jonin, and P. F. Brevet, "Wavelength dependence of the retardation effects in silver nanoparticles followed by polarization resolved hyper rayleigh scattering," Chem. Phys. Lett. **415**, 246–250 (2005).
11. J. Nappa, G. Revillod, I. Russier-Antoine, E. Benichou, C. Jonin, and P. F. Brevet, "Electric dipole origin of the second harmonic generation of small metallic particles," Phys. Rev. B **71**, 165407 (2005).
12. D. de Ceglia, M. A. Vincenti, C. De Angelis, A. Locatelli, J. W. Haus, and M. Scalora, "Role of antenna modes and field enhancement in second harmonic generation from dipole nanoantennas," Opt. Express **23**, 1715–1729 (2015).
13. A. Bouhelier, M. Beversluis, A. Hartschuh, and L. Novotny, "Near-field second-harmonic generation induced by local field enhancement," Phys. Rev. Lett. **90**, 013903 (2003).
14. A. Nahata, R. A. Linke, T. Ishi, and K. Ohashi, "Enhanced nonlinear optical conversion from a periodically nanostructured metal film," Opt. Lett. **28**, 423–425 (2003).
15. M. W. Klein, M. Wegener, N. Feth, and S. Linden, "Experiments on second- and third-harmonic generation from magnetic metamaterials: erratum," Opt. Express **16**, 8055 (2008).
16. S. Kujala, B. K. Canfield, M. Kauranen, Y. Svirko, and J. Turunen, "Multipole interference in the second-harmonic optical radiation from gold nanoparticles," Phys. Rev. Lett. **98**, 167403 (2007).
17. M. Celebrano, X. Wu, M. Baselli, S. Großmann, P. Biagioni, A. Locatelli, C. De Angelis, G. Cerullo, R. Osellame, B. Hecht, Lamberto Duò, Franco Ciccacci, and Marco Finazzi, "Mode matching in multiresonant plasmonic nanoantennas for enhanced second harmonic generation," Nat. Nanotechnol. **10**, 412–417 (2015).
18. B. K. Canfield, H. Husu, J. Laukkanen, B. Bai, M. Kuittinen, J. Turunen, and M. Kauranen, "Local field asymmetry drives second-harmonic generation in noncentrosymmetric nanodimers," Nano Lett. **7**, 1251–1255 (2007).
19. I. Ledoux, J. Zyss, J. Siegel, J. Brienne, and J. Lehnb, "Second-harmonic generation from non-dipolar non-centrosymmetric aromatic charge-transfer molecules," Chem. Phys. Lett. **172**, 440–444 (1990).
20. R. Wortmann, C. Glania, P. Kramer, R. Matschiner, J. J. Wolff, S. Kraft, B. Treptow, E. Barbu, D. Langle, and G. Gorlitz, "Nondipolar structures with threefold symmetry for nonlinear optics," Chem. -Eur. J. **3**, 1765–1773 (1997).
21. S. Stadler, F. Feiner, C. Brauchle, S. Brandl, and R. Gompper, "Determination of the first hyperpolarizability of four octupolar molecules and their dipolar subunits via hyper-rayleigh scattering in solution," Chem. Phys. Lett. **245**, 292–296 (1995).
22. I. R. Whittall, M. G. Humphrey, S. Houbrechts, J. Maes, A. Persoons, S. Schmid, and D. C. Hockless, "Organometallic complexes for nonlinear optics. 14. syntheses and second-order nonlinear optical properties of ruthenium, nickel and gold $\sigma$-acetylides of 1,3,5-triethynylbenzene: X-ray crystal structures of 1-(HC ≡ C)-3,5-$C_6H_3$ ( *trans*-C≡ CRuCl(dppm)$_2$)$_2$ and 1,3,5-$C_6H_3$(C ≡ CAu($PPh_3$))$_3$," J. Orgonomet. Chem. **544**, 277–283 (1997).
23. B. del Rey, U. Keller, T. Torres, G. Rojo, F. Agulló-López, S. Nonell, C. Martí, S. Brasselet, I. Ledoux, and J. Zyss, "Synthesis and nonlinear optical, photophysical, and electrochemical properties of subphthalocyanines," J. Am. Chem. Soc. **120**, 12808–12811 (1998).
24. H. Shen, N. Nguyen, D. Gachet, V. Maillard, T. Toury, and S. Brasselet, "Nanoscale optical properties of metal nanoparticles probed by second harmonic generation microscopy," Opt. Express **21**, 12318–12326 (2013).
25. S. Kujala, B. K. Canfield, M. Kauranen, Y. Svirko, and J. Turunen, "Multipole interference in the second-harmonic optical radiation from gold nanoparticles," Phys. Rev. Lett. **98**, 167403 (2007).
26. R. Czaplicki, H. Husu, J. Laukkanen, M. Kuittinen, and M. Kauranen, *Nonlinear, Tunable and Active Metamaterials* (Springer International Publishing, Cham, 2015), Chap. 6, pp. 105–116.
27. N. G. Bastús, J. Piella, and V. Puntes, "Quantifying the sensitivity of multipolar (dipolar, quadrupolar, and octapolar) surface plasmon resonances in silver nanoparticles: The effect of size, composition, and surface coating," Langmuir **32**, 290–300 (2016).
28. H. Shen, N. Guillot, J. Rouxel, M. Lamy de la Chapelle, and T. Toury, "Optimized plasmonic nanostructures for improved sensing activities," Opt. Express **20**, 21278–21290 (2012).
29. C. I. Valencia and E. R. Méndez, "Second-harmonic generation in the scattering of light by two-dimensional particles," J. Opt. Soc. Am. B **20**, 2150–2161 (2003).
30. W. Hübner, K. H. Bennemann, and K. Böhmer, "Theory for the nonlinear optical response of transition metals: Polarization dependence as a fingerprint of the electronic structure at surfaces and interfaces," Phys. Rev. B **50**, 17597 (1994).
31. G. Petrocelli, S. Martellucci, and R. Francini, "Wavelength dependence of second-harmonic generation at the copper

Optics EXPRESS

surface," Appl. Phys. A **56**, 263–266 (1993).
32. B. Richards, E. Wolf, and D. Gabor, "Electromagnetic diffraction in optical systems. ii. structure of the image field in an aplanatic system," P. Roy. Soc. Lond. A Mat. **253**, 358–379 (1959).
33. J. R. Rouxel and T. Toury, "Optical multipolar spread functions of an aplanatic imaging system," J. Opt. **18**, 075002 (2016).
34. J. Enderlein, "Theoretical study of detection of a dipole emitter through an objective with high numerical aperture," Opt. Lett. **25**, 634–636 (2000).
35. L. Novotny and B. Hecht, *Principles of Nano-Optics* (Cambridge University, 2006).
36. H. Shen, J. Rouxel, N. Guillot, M. Lamy de la Chapelle, and T. Toury, "Light polarization properties of three fold symmetry gold nanoparticles: Model and experiments," C. R. Phys. **13**, 830–836 (2012).
37. S. Brasselet and J. Zyss, "Multipolar molecules and multipolar fields: probing and controlling the tensorial nature of nonlinear molecular media," J. Opt. Soc. Am. B **15**, 257–288 (1998).
38. J. Jerphagnon, "Invariants of the third-rank cartesian tensor: Optical nonlinear susceptibilities," Phys. Rev. B **2**, 1091–1098 (1970).
39. J. D. Jackson, *Classical Electrodynamics* (Wiley, 1998).
40. D. Varshalovich, A. Moskalev, and V. Khersonskii, *Quantum Theory of Angular Momentum* (World Scientific Pub Co, 1988).
41. M. Kauranen and A. V. Zayats, "Nonlinear plasmonics," Nat. Photonics **6**, 737–748 (2012).
42. A. B. Evlyukhin, C. Reinhardt, and B. N. Chichkov, "Multipole light scattering by nonspherical nanoparticles in the discrete dipole approximation," Phys. Rev. B **84**, 235429 (2011).
43. M. Guasoni, L. Carletti, D. Neshev, and C. De Angelis, "Theoretical model for pattern engineering of harmonic generation in all-dielectric nanoantennas," IEEE J. Quantum Elect. **53**, 1–5 (2017).
44. L. Carletti, D. Rocco, A. Locatelli, C. De Angelis, V. Gili, M. Ravaro, I. Favero, G. Leo, M. Finazzi, L. Ghirardini, M. Celebrano, G. Marino, and A. V. Zayats, "Controlling second-harmonic generation at the nanoscale with monolithic algaas-on-alox antennas," Nanotechnol. **28**, 114005 (2017).
45. J. Grand, S. Kostcheev, J.-L. Bijeon, M. Lamy de la Chapelle, P.-M. Adam, A. Rumyantseva, G. Lerondel, and P. Royer, "Optimization of sers-active substrates for near-field raman spectroscopy," Synth. Met. **139**, 621–624 (2003).
46. S. Brasselet, V. L. Floc'h, F. Treussart, J.-F. Roch, and J. Zyss, "In situ diagnostics of the crystalline nature of single organic nanocrystals by nonlinear microscopy," Phys. Rev. Lett. **92**, 207401 (2004).
47. H. Vanherzeele and J. D. Bierlein, "Magnitude of the nonlinear-optical coefficients of ktiopo4," Opt. Lett. **17**, 982–984 (1992).
48. E. Delahaye, N. Tancrez, T. Yi, I. Ledoux, J. Zyss, S. Brasselet, and R. Clément, "Second harmonic generation from individual hybrid $MnPS_3$," Chem. Phys. Lett. **429**, 533–537 (2006).
49. R. W. Boyd, *Nonlinear Optics* (Elsevier, 2008).
50. J. L. Oudar and D. S. Chemla, "Hyperpolarizabilities of the nitroanilines and their relations to the excited state dipole moment," J. Chem. Phys. **66**, 2664–2668 (1977).